Supplementary Material for "Controlling anomalous Hall conductivity using antiferromagnetic configurations in GdPtBi"

Fiqhri Heda Murdaka[a,b], Yusuf Wicaksono[c], Edi Suprayoga[d], Abdul-Muizz Pradipto[e], Bambang Prijamboedi[e], Isao Watanabe[b], Agustinus Agung Nugroho[e]

[a]Graduate Program of Physics, Institut Teknologi Bandung, Jl. Ganesha No 10, Bandung, 40132, Jawa Barat, Indonesia
[b]Nuclear Structure Research Group, Nishina Center for Accelerator-Based Science, RIKEN, 2-1 Hirosawa, Wako, 351-0198, Saitama, Japan
[c]RIKEN Cluster for Pioneering Research (CPR), 2-1 Hirosawa, Wako, 351-0198, Saitama, Japan
[d]Research Center for Quantum Physics, National Research and Innovation Agency (BRIN), Jl. Kawasan PUSPIPTEK Serpong, Tangerang Selatan, 15214, Banten, Indonesia
[e]Faculty of Mathematics and Natural Sciences, Institut Teknologi Bandung, Jl. Ganesha No 10, Bandung, 40132, Jawa Barat, Indonesia

This supplementary material (SM) provides additional results supporting the explanations presented in the main text. The SM is divided into six sections. Section S.1 discusses convergence tests for the Hubbard correction applied to the Gd f-orbital, the calculation range for the dipolar magnetic field, and the k-mesh used in anomalous Hall conductivity calculations. Section S.2 presents the band structure along $\Gamma - Z - F - \Gamma - L$ and the orbital density of states (DOSs) for FM [111] and AFM$_{\perp,\phi=0°,15°,30°}$. Section S.3 provides details of the k-resolved DOS for various ϕ values in AFM$_\perp$. Section S.4 includes the complete band spin and orbital angular momentum (OAM) projections along $Z - \Gamma - Z$ and $F - \Gamma - F$. Section S.5 lists the energies, positions, and chiralities of nodal points for FM and AFM$_{\perp,\phi=0°,15°,30°}$ configurations. In the end, Section S.6 presents the Fermi surface and Fermi lines of AFM$_\perp$.

S.1. Calculation parameter optimization

S.1.1. Hubbard correction of Gd f-orbital

The Hubbard correction value for the Gd f-orbital was determined by comparing the Gd magnetic moment obtained from DFT calculations with the value reported in neutron diffraction studies[1], which is $7.65\,\mu_B$. As illustrated in Figure S.1, the magnetic moment of Gd atoms saturates at $7.06\,\mu_B$. Taking into account a tolerance of $0.006\mu_B$, a $+U$ value of 10 eV is considered an appropriate Hubbard correction.
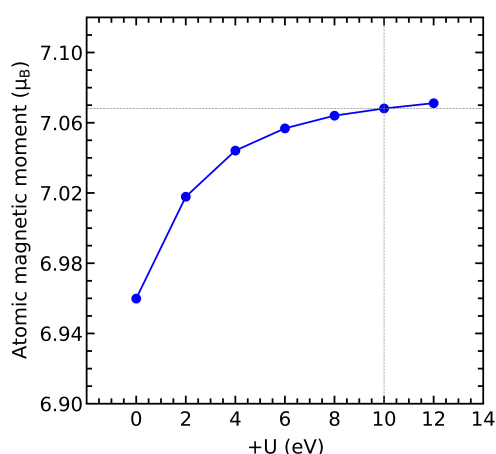

Figure S.1: Magnetic moment of Gd atoms converged within tolerance of $0.006\,\mu_B$ at $+U = 10eV$

The influence of $+U$ on the f-orbital electrons was also analyzed through the partial density of states (PDOS). A comparison was made between the $+U$ value of 4.6 eV suggested in the

literature [2] and the selected value of 10 eV. The PDOS results indicate that the f orbital states remain localized and positioned far from the Fermi energy for both $+U$ values, as shown in Figure S.2. This ensures that the chosen Hubbard correction does not affect the calculations of topological properties and AHC, which are primarily concentrated around the Fermi energy.
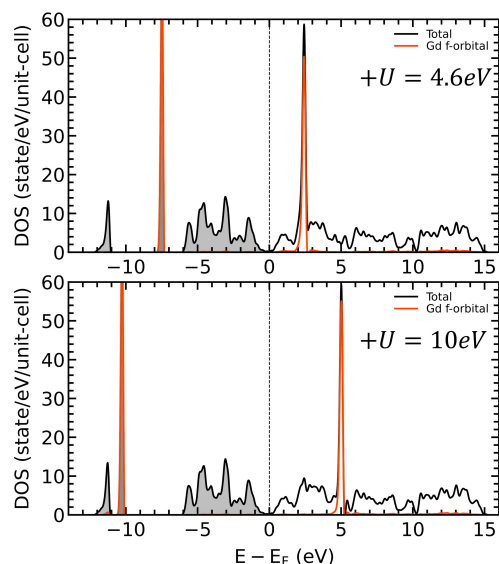

Figure S.2: PDOS of Gd f-orbital for $+U = 4.6eV$ and $10eV$

S.1.2. Dipolar Magnetic Field Calculation Range

The dipolar magnetic field at the muon site, calculated using equation (1) from the main text, was determined based

on Gd atoms with magnetic moments obtained from DFT calculations. These atoms are located within a specified radius sphere. The sphere's radius was optimized to ensure convergence within a specified relative tolerance of 0.1% and tested for the $AFM_{\perp,\phi=30°}$ configuration with the muon site depicted in Figure 2 of the main text. Convergence within the tolerance was achieved at a radius of 100 Å for both A and B muon sites, as shown in Figure S.3.
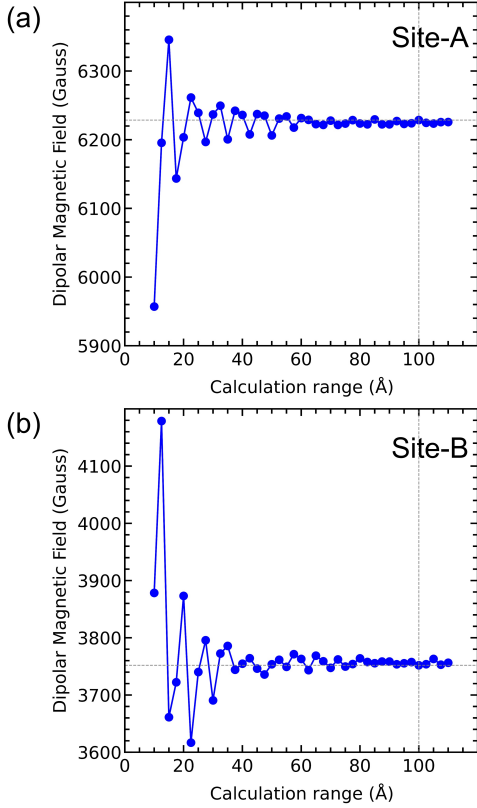
(a)

(b)

Figure S.3: Convergence test of magnetic dipole field calculation in GdPtBi with $AFM_{\perp,\phi=30°}$ configuration for muon-site at (a) A-site and (b) B-site

S.1.3. Anomalous Hall Conductivity k-mesh convergence test

A k-mesh convergence test for the Anomalous Hall Conductivity (AHC) calculation (σ_{xy}) was performed using the Kubo formula provided in the main text equation (5). With a relative tolerance of 2.75%, the AHC values converge at a $100 \times 100 \times 100$ k-mesh, as shown in Figure S.4.

S.2. Band structure and density of states

The band structures of GdPtBi for FM, $AFM_{\perp,\phi=0°}$, $AFM_{\perp,\phi=15°}$, and $AFM_{\perp,\phi=30°}$ are presented in Figure S.5. The FM configuration displays a distinct band structure due to spin splitting caused by the Stoner gap between majority and minority spins. In contrast, the band structures of $AFM_{\perp,\phi=15°}$ and $AFM_{\perp,\phi=30°}$ closely resemble $AFM_{\perp,\phi=0°}$, with the exception of a small band splitting near the Γ point, as shown in the Supplementary Material section S.4. Moreover, the orbital-projected
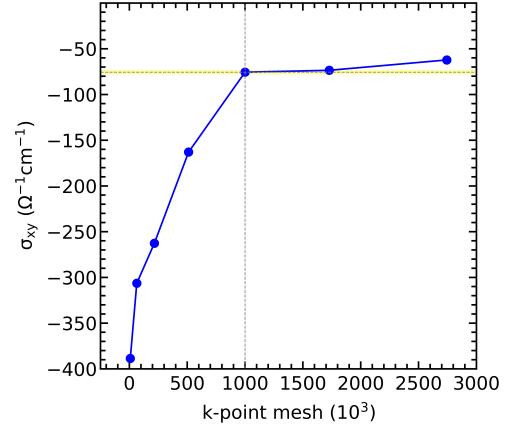
Figure S.4: Convergence test of AHC, the value of σ_{xy} is converge at $100 \times 100 \times 100$ with relative tolerance of 2.75% shown in yellow area

densities of states (DOSs) within the energy range of -2 to 2 eV reveal a significant contribution from both p- and d-orbitals, particularly the d-orbitals of the Gd atom and the p-orbitals of the Bi atom.

S.3. k-resolved density of states

The dominant orbital contribution near the Fermi energy for $AFM_{\perp,\phi=0°}$, $AFM_{\perp,\phi=15°}$, and $AFM_{\perp,\phi=30°}$ mainly arises from the Gd atom, as illustrated by the k-resolved DOS in Figure S.6.

S.4. Band spin and orbital angular momentum projection

The band spin and orbital angular momentum (OAM) projections for $AFM_{\perp,\phi=0°}$, $AFM_{\perp,\phi=15°}$, and $AFM_{\perp,\phi=30°}$ along $Z(\frac{1}{2},\frac{1}{2},\frac{1}{2}) - \Gamma(0,0,0) - Z(-\frac{1}{2},-\frac{1}{2},-\frac{1}{2})$ are shown in Figures S.7, S.8, S.9, and for along $F(\frac{1}{2},\frac{1}{2},0) - \Gamma(0,0,0) - F(-\frac{1}{2},-\frac{1}{2},0)$ are presented in Figures S.10, S.11, S.12, respectively. A progressive band splitting is observed from $AFM_{\perp,\phi=0°}$ to $AFM_{\perp,\phi=30°}$ which is attributed to the increasing strength of spin-orbit coupling (SOC). It is also notable that along $Z(\frac{1}{2},\frac{1}{2},\frac{1}{2}) - \Gamma(0,0,0) - Z(-\frac{1}{2},-\frac{1}{2},-\frac{1}{2})$, $\langle S_x \rangle$ is the dominant component in $AFM_{\perp,\phi=0°}$, while $\langle S_z \rangle$ becomes dominant in both $AFM_{\perp,\phi=15°}$ and $AFM_{\perp,\phi=30°}$.

S.5. Nodal point energy, position, and chirality

S.5.1. FM structure

Nodal points in the ferromagnetic (FM) structure are identified as Weyl points with their positions, energies, and chiralities listed in Table S.1. The Berry curvature flux around the Weyl points in the $k_1 = k_x + k_y$ versus k_z plane is depicted in Figure S.13, where positive chirality acts as a source of Berry curvature, and negative chirality serves as a sink.
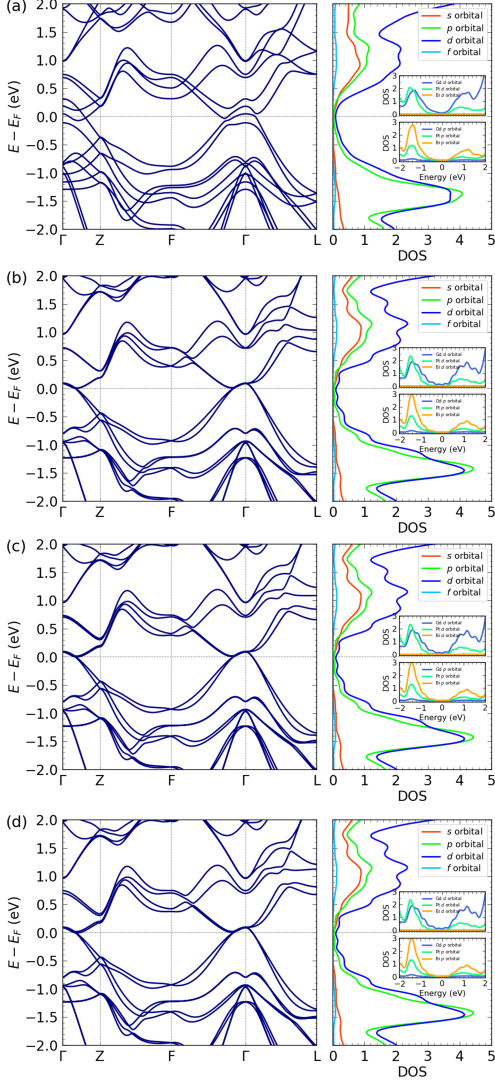
2

Figure S.5: Band structure at $\Gamma - Z - F - \Gamma - L$ and DOSs of (a) FM, (b) AFM$_{\perp,\phi=0°}$, (c) AFM$_{\perp,\phi=15°}$, and (d) AFM$_{\perp,\phi=30°}$

S.5.2. AFM$_{\perp,\phi=0°}$ structure

Nodal points in the AFM$_{\perp,\phi=0°}$ structure are classified as triple points, with their positions, energies, and chiralities listed in Table S.2.

S.5.3. AFM$_{\perp,\phi=15°}$ structure

Nodal points in the AFM$_{\perp,\phi=15°}$ structure are classified as triple points, with their positions, energies, and chiralities listed in Table S.3.

S.5.4. AFM$_{\perp,\phi=30°}$ structure

Nodal points in the AFM$_{\perp,\phi=30°}$ structure are classified as triple points, with their positions, energies, and chiralities listed in Table S.4.
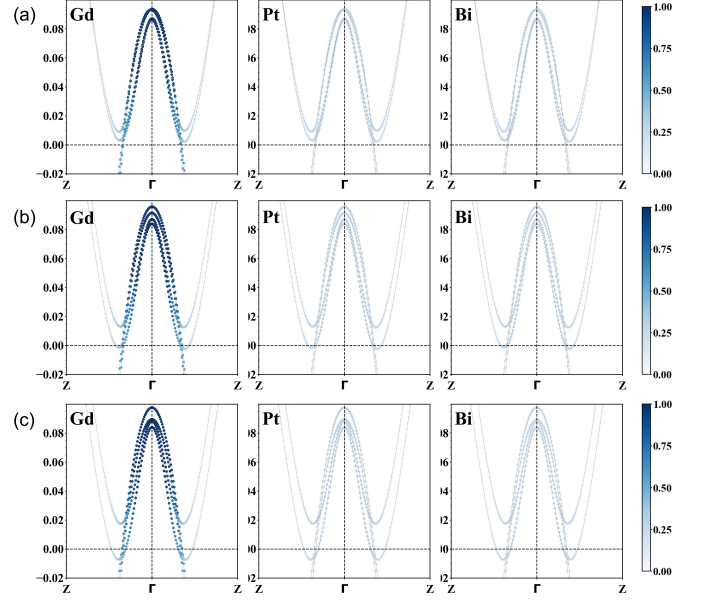

Figure S.6: k-resolved density of states for (a) AFM$_{\perp,\phi=0°}$, (b) AFM$_{\perp,\phi=15°}$, and (c) AFM$_{\perp,\phi=30°}$.

Table S.1: Weyl point energy, position, and chirality for FM structure

Energy (meV)	k_x	k_y	k_z	Chirality
-10	-0.079	-0.0786	-0.0785	+1
	0.0786	0.0788	0.0788	-1
-24	0.066	0.0716	-0.0613	+1
	0.0716	-0.0614	0.0661	+1
	-0.0612	0.0657	0.0716	+1
	0.0609	-0.0716	-0.0654	-1
	-0.0716	-0.0658	0.0611	-1
	-0.0664	0.0615	-0.0717	-1

S.6. Fermi Surface

The Fermi surface and corresponding Fermi lines contributing to the AHC value at the Fermi energy for AFM$_{\perp}$ are shown in Figure S.14. Based on closer inspection of the Fermi surface, as prescribed by Wang *et al.* [3], the σ_{xy} components in AFM$_{\perp,\phi=15°}$ and AFM$_{\perp,\phi=30°}$ arise from the Berry phase contributions of the hole-pocket loops in the Fermi surface.

References

[1] R. Müller, N. Lee-Hone, L. Lapointe, D. Ryan, T. Pereg-Barnea, A. Bianchi, Y. Mozharivskyj, R. Flacau, Magnetic structure of gdbipt: A candidate antiferromagnetic topological insulator, Physical Review B 90 (4) (2014) 041109.

[2] W. Xun, C. Wu, H. Sun, W. Zhang, Y.-Z. Wu, P. Li, Coexisting magnetism, ferroelectric, and ferrovalley multiferroic in stacking-dependent two-dimensional materials, Nano letters 24 (11) (2024) 3541–3547.

[3] X. Wang, D. Vanderbilt, J. R. Yates, I. Souza, Fermi-surface calculation of the anomalous hall conductivity, Physical Review B—Condensed Matter and Materials Physics 76 (19) (2007) 195109.
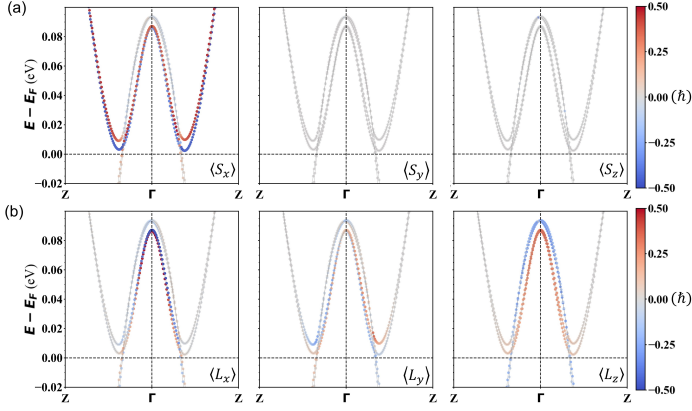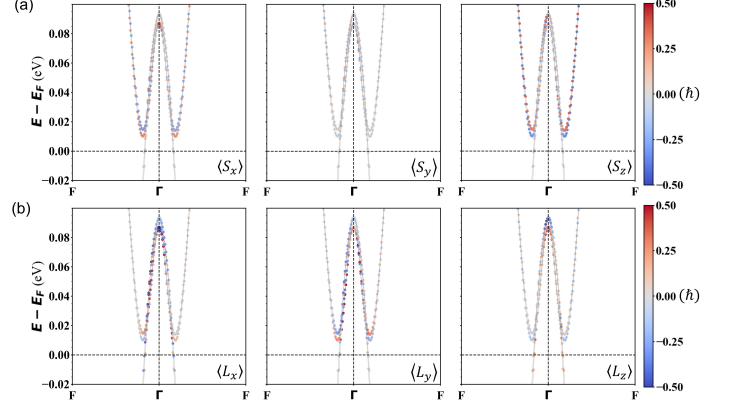
Figure S.7: (a) band spin projection and (b) band orbital angular momentum projection for $AFM_{\perp,\phi=0°}$ along $Z(\frac{1}{2},\frac{1}{2},\frac{1}{2}) - \Gamma(0,0,0) - Z(-\frac{1}{2},-\frac{1}{2},-\frac{1}{2})$.

Figure S.10: (a) band spin projection and (b) band orbital angular momentum projection for $AFM_{\perp,\phi=0°}$ .along $F\left(\frac{1}{2},\frac{1}{2},0\right) - \Gamma(0,0,0) - F\left(-\frac{1}{2},-\frac{1}{2},0\right)$.
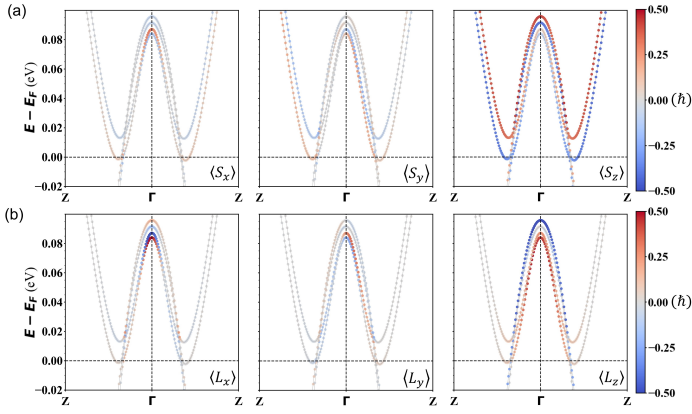

Figure S.8: (a) band spin projection and (b) band orbital angular momentum projection for $AFM_{\perp,\phi=15°}$ along $Z(\frac{1}{2},\frac{1}{2},\frac{1}{2}) - \Gamma(0,0,0) - Z(-\frac{1}{2},-\frac{1}{2},-\frac{1}{2})$
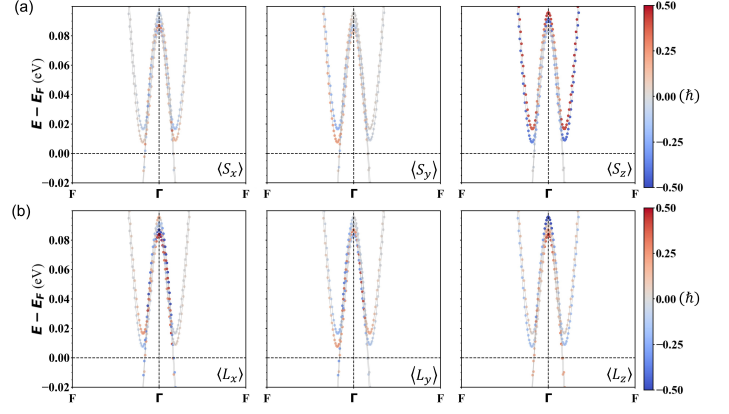

Figure S.11: (a) band spin projection and (b) band orbital angular momentum projection for $AFM_{\perp,\phi=15°}$ along $F\left(\frac{1}{2},\frac{1}{2},0\right) - \Gamma(0,0,0) - F\left(-\frac{1}{2},-\frac{1}{2},0\right)$.

Figure S.9: (a) band spin projection and (b) band orbital angular momentum projection for $AFM_{\perp,\phi=30°}$. along along $Z(\frac{1}{2},\frac{1}{2},\frac{1}{2}) - \Gamma(0,0,0) - Z(-\frac{1}{2},-\frac{1}{2},-\frac{1}{2})$.

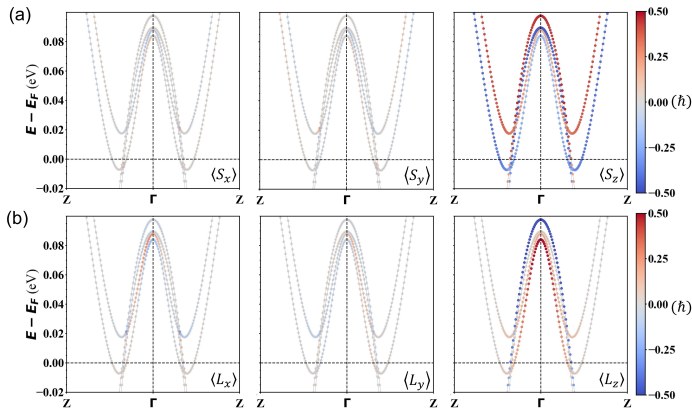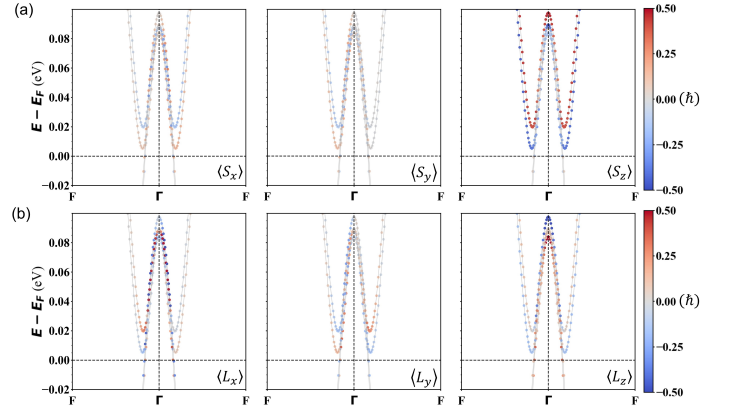Figure S.12: (a) band spin projection and (b) band orbital angular momentum projection for $AFM_{\perp,\phi=30°}$ along $F\left(\frac{1}{2},\frac{1}{2},0\right) - \Gamma(0,0,0) - F\left(-\frac{1}{2},-\frac{1}{2},0\right)$.
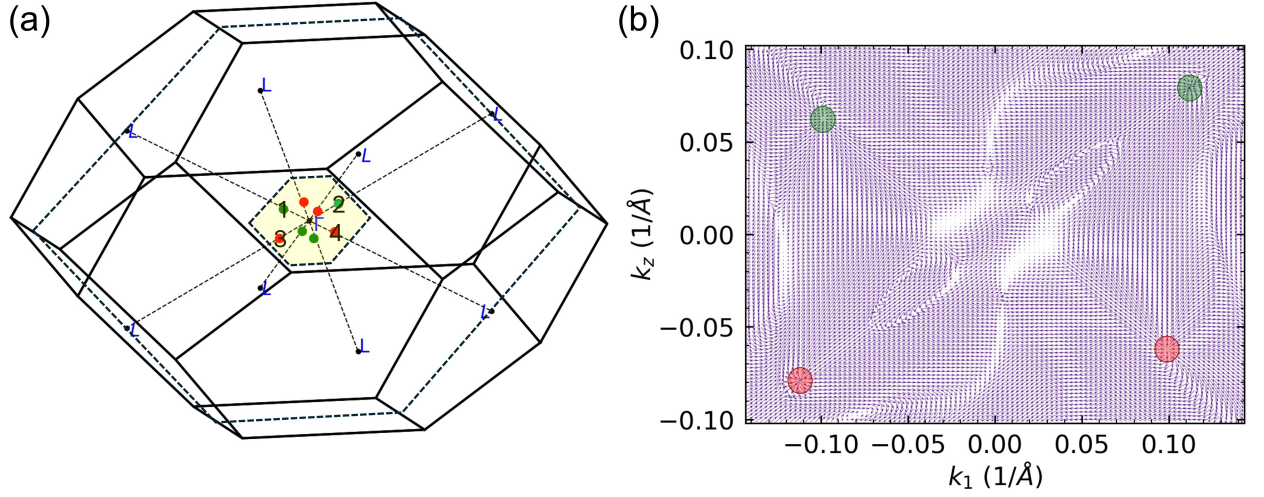
Figure S.13: (a) Weyl point with + (red) and − (green) chirality of FM GdPtBi inside Brillouin zone and (b) Berry curvature field in a plane which slice the numbered Weyl point (yellow plane).

Table S.2: Triple point energy, position and chirality for AFM$_\perp$, $\phi = 0°$ structure

Energy (meV)	k_x	k_y	k_z	Chirality
7	0.0009	0.0	-0.07	+1
4	0.0002	0.0001	0.072	+1
21	-0.0005	0.0597	-0.0214	+1
18	0.0515	-0.0301	-0.0225	+1
23	0.0496	0.0288	0.0205	+1
6	-0.0007	-0.0001	-0.0708	-1
7	-0.0001	0.0002	0.0697	-1
18	0.0527	0.0303	0.0215	-1
18	0.0515	-0.0294	-0.0208	-1
20	-0.0011	0.0606	-0.0211	-1

Table S.4: Triple point energy, position and chirality for AFM$_\perp$, $\phi = 30°$ structure

Energy (meV)	k_x	k_y	k_z	Chirality
23	-0.0002	-0.0001	-0.0619	+1
11	0.0558	-0.0315	-0.0228	+1
-5	0.0005	0.0003	0.0771	+1
11	0.0557	0.0312	0.0225	+1
23	0.0003	0.0001	0.0616	-1
-3	-0.0002	-0.0004	-0.0762	-1
24	0.0499	-0.0283	-0.0199	-1
8	0.0566	0.032	0.0231	-1

Table S.3: Triple point energy, position and chirality for AFM$_\perp$, $\phi = 15°$ structure

Energy (meV)	k_x	k_y	k_z	Chirality
20	0.0001	-0.0583	0.0202	+1
17	-0.0004	-0.0004	-0.0655	+1
5	0.0006	0.0	0.072	+1
20	-0.0514	-0.0293	-0.0211	+1
19	0.0	0.059	-0.0217	+1
23	0.0498	0.0276	0.02	+1
19	0.0004	-0.0593	0.021	-1
-1	0.0	0.0006	-0.0749	-1
11	0.0007	0.0002	0.0685	-1
17	-0.0529	-0.0313	0.0215	-1
20	0.051	0.03	0.0215	-1
7	-0.0002	0.0648	-0.0231	-1
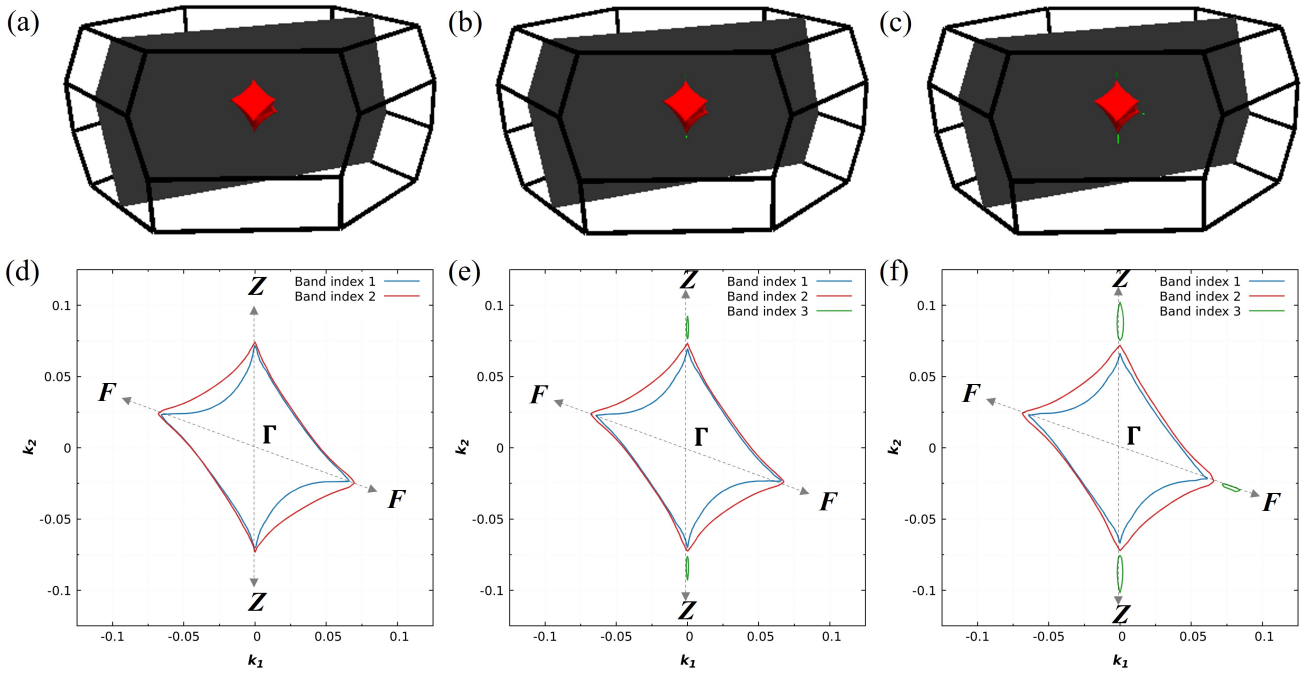
Figure S.14: Fermi surface of (a) AFM$_{\perp,\phi=0°}$, (b) AFM$_{\perp,\phi=15°}$, and (c) AFM$_{\perp,\phi=30°}$. Panels (d), (e), and (f) show the corresponding Fermi lines on the gray planes indicated in (a), (b), and (c), respectively.